J. Fluid Mech. (2005), *vol.* 538, *pp.* 223–244.
doi:10.1017/S0022112005005446 Printed in the United Kingdom

Thermocapillary long waves in a liquid film flow. Part 2. Linear stability and nonlinear waves

By B. SCHEID[1,2], C. RUYER-QUIL[2], S. KALLIADASIS[3]†, M. G. VELARDE[4] AND R. Kh. ZEYTOUNIAN[5]

[1]Chimie-Physique E.P., Université Libre de Bruxelles, C.P. 165/62, 1050 Brussels, Belgium

[2]Laboratoire FAST, UMR 7608, CNRS, Universités P. et M. Curie et Paris Sud, Bât. 502, Campus Universitaire, 91405 Orsay Cedex, France

[3]Department of Chemical Engineering, University of Leeds, Leeds LS2 9JT, UK

[4]Insituto Pluridisciplinar, Universidad Complutense de Madrid, Paseo Juan XXIII, n. 1, E-28040 Madrid, Spain

[5]Université des Sciences et Technologies de Lille, 59655 Villeneuve d'Asq cédex, France

bscheid@ulb.ac.be; ruyer@fast.u-psud.fr; s.kalliadasis@imperial.ac.uk; velarde@fluidos.pluri.ucm.es; zeytounian@aol.com

(Received 16 February 2004 and in revised form 23 March 2005)

We analyse the regularized reduced model derived in Part 1 (Ruyer-Quil *et al.* 2005). Our investigation is two-fold: (i) we demonstrate that the linear stability properties of the model are in good agreement with the Orr–Sommerfeld analysis of the linearized Navier–Stokes/energy equations; (ii) we show the existence of nonlinear solutions, namely single-hump solitary pulses, for the widest possible range of parameters. We also scrutinize the influence of Reynolds, Prandtl and Marangoni numbers on the shape, speed, flow patterns and temperature distributions for the solitary waves obtained from the regularized model. The hydrodynamic and Marangoni instabilities are seen to reinforce each other in a non-trivial manner. The transport of heat by the flow has a stabilizing effect for small-amplitude waves but promotes the instability for large-amplitude waves when a recirculating zone is present. Nevertheless, in this last case, by increasing the shear in the bulk and thus the viscous dissipation, increasing the Prandtl number decreases the amplitude and speed of the waves.

1. Introduction

The present study is devoted to the problem of long-wave instabilities – namely hydrodynamic H- and thermocapillary S-modes (Goussis & Kelly 1991) – and concomitant formation of solitary waves on the surface of a film falling down a uniformly heated plane. In Part 1 (Ruyer-Quil *et al.* 2005), we developed a low-dimensional model capable of capturing these phenomena in a wide range of Reynolds numbers, i.e. in both drag–gravity and drag–inertia regimes (Ooshida 1999). The model, which also takes into account the second-order dissipative effects that can play an important role in the drag–inertia regime (Ruyer-Quil & Manneville 2000), was referred to as the 'second-order regularized reduced model'. It is rewritten here

† Present address: Department of Chemical Engineering, Imperial College, London SW7 2AZ, UK.

for ease of presentation:

$$\partial_t h = -\partial_x q, \tag{1.1a}$$

$$\begin{aligned}\partial_t q = {} & \frac{9}{7}\frac{q^2}{h^2}\partial_x h - \frac{17}{7}\frac{q}{h}\partial_x q \\ & + \left\{\frac{5}{6}h - \frac{5}{2}\frac{q}{h^2} + 4\frac{q}{h^2}(\partial_x h)^2 - \frac{9}{2h}\partial_x q\partial_x h - 6\frac{q}{h}\partial_{xx}h + \frac{9}{2}\partial_{xx}q\right. \\ & \left. - \frac{5}{6}\cot\beta\, h\partial_x h + \frac{5}{6}\Gamma h\partial_{xxx}h - Ma\left(\frac{5}{4}\partial_x\theta - \frac{1}{224}hq\partial_{xx}\theta\right)\right\} \\ & \times\left(1 - \frac{1}{70}q\partial_x h + Ma\frac{5}{56h}\partial_x\theta\right)^{-1},\end{aligned} \tag{1.1b}$$

$$\begin{aligned}Pr\partial_t\theta = {} & 3\frac{(1-\theta-Bi\,h\theta)}{h^2} + Pr\left[\frac{7}{40}\frac{(1-\theta)}{h}\partial_x q - \frac{27}{20}\frac{q}{h}\partial_x\theta\right] \\ & + \left(1-\theta-\frac{3}{2}Bih\theta\right)\left(\frac{\partial_x h}{h}\right)^2 + \frac{\partial_x h\partial_x\theta}{h} + (1-\theta)\frac{\partial_{x^2}h}{h} + \partial_{xx}\theta,\end{aligned} \tag{1.1c}$$

where the Kapitza, Marangoni, Biot and Prandtl numbers are defined as

$$\Gamma = \frac{\sigma(T_0)}{\rho\nu^{4/3}(g\sin\beta)^{1/3}}, \quad Ma = \frac{-\mathrm{d}\sigma/\mathrm{d}T|_{T_0}(T_\mathrm{w}-T_0)}{\rho\nu^{4/3}(g\sin\beta)^{1/3}}, \quad Bi = \frac{q_0\,\nu^{2/3}}{K(g\sin\beta)^{1/3}}, \quad Pr = \frac{\nu}{\kappa},$$

and where σ is the surface tension, ρ the density, ν the viscosity, $g\sin\beta$ the streamwise gravity component, q_0 the heat transfer coefficient of the liquid–gas interface, K the thermal conductivity of the liquid, κ the thermal diffusivity, T_w the wall temperature and T_0 a reference temperature, taken here as the ambient temperature T_a. This set of parameters is completed by the flat-film thickness h_N or equivalently the Reynolds number

$$Re = \frac{g\sin\beta h_\mathrm{N}^3}{3\nu^2} = \frac{\bar{h}_\mathrm{N}^3}{3} \tag{1.2}$$

while the product $Pe = Pr\,Re$ defines the Péclet number. A bar in (1.2) has been introduced to distinguish between dimensional and dimensionless quantities.

In § 2, the linear stability properties of (1.1) are examined and compared to results from Orr–Sommerfeld analysis of the full Navier–Stokes/energy equations, the Benney expansion, as well as the full-size model of reduced dimensionality (see Part 1), from which (1.1) was derived through a regularization procedure. In § 3 we scrutinize the effect of the Reynolds, Prandtl and Marangoni numbers on the shape, speed, temperature distribution and flow patterns for the single-hump solitary waves obtained from (1.1). We also explore the interaction between the S- and H-modes in the nonlinear regime. Finally, a conclusion and discussion is offered in § 4.

2. Linear stability results

We now examine the linear stability of the basic Nusselt flow and we compare the results obtained from the regularized reduced model to those obtained from the Orr–Sommerfeld eigenvalue problem of the full Navier–Stokes/energy equations. This eigenvalue problem was first formulated and solved by Goussis & Kelly (1991) and the reader is referred to this study for details. It is also instructive here to include the linear stability analysis obtained from the first-order model (§ 4.1 in Part 1), boundary-layer equation (§ 3 in Part 1) and full-size second-order model

(Appendix A in Part 1). The dispersion relation corresponding to (1.1) can be obtained by introducing perturbations to the flat-film solution in the form of normal modes with wavenumber $\tilde{k}$ and frequency $\tilde{\omega}$ (here we focus on temporal stability so that the wavenumber is real and the frequency complex)

$$\begin{pmatrix} h \\ q \\ \theta \end{pmatrix} = \begin{pmatrix} \bar{h}_{\mathrm{N}} \\ \bar{h}_{\mathrm{N}}^3/3 \\ 1/(1+Bi\,\bar{h}_{\mathrm{N}}) \end{pmatrix} + \varepsilon \begin{pmatrix} 1 \\ A_q \\ A_\theta \end{pmatrix} \exp\{\mathrm{i}(\tilde{k}x - \tilde{\omega}t)\} \tag{2.1}$$

in (1.1) and then linearize for $\varepsilon \ll 1$. For the resulting system of linear algebraic equations to have non-trivial solutions, it is necessary and sufficient that its principal determinant be equal to zero. Similarly, substituting (2.1), $s_i = \varepsilon A_{s_i} \exp\{\mathrm{i}(\tilde{k}x - \tilde{\omega}t)\}$ and $t_i = \varepsilon A_{t_i} \exp\{\mathrm{i}(\tilde{k}x - \tilde{\omega}t)\}$ in the full-size model (see Appendix A of Part 1) gives its dispersion relation.

To compare our linear stability analysis with the one performed by Kalliadasis *et al.* (2003), we must non-dimensionalize the length scales with the Nusselt film thickness h_{N}. Still utilizing bars to distinguish dimensional and dimensionless quantities when needed, we are thus led to the transformation $\tilde{k} = k/\bar{h}_{\mathrm{N}}$ and $\tilde{\omega} = \bar{h}_{\mathrm{N}}\omega$, where $\bar{h}_{\mathrm{N}} = (3Re)^{1/3}$ from (1.2). The phase speed $\tilde{c} = \tilde{\omega}/\tilde{k}$ is transformed to $\tilde{c} = \bar{h}_{\mathrm{N}}^2 c$. The averaged velocity of the flat-film solution is then $1/3$ with this scaling. A different set of parameters based on the Nusselt flat-film solution therefore appears:

$$Ma_{\Delta T} = \frac{-\mathrm{d}\sigma/\mathrm{d}T|_{T_0}\,\Delta T}{\rho h_{\mathrm{N}}^2 g \sin\beta}, \quad We = \frac{\sigma(T_{\mathrm{a}})}{\rho g h_{\mathrm{N}}^2 \sin\beta}, \quad B = \frac{q_0 h_{\mathrm{N}}}{K}, \tag{2.2}$$

where ΔT is the temperature difference across the uniform fluid layer of thickness h_{N}. This set is completed by the definition of the Reynolds number given in (1.2). These are effectively the parameters adopted by Kalliadasis *et al.* (2003) except that these authors expressed the Weber number as the ratio of surface tension over inertia forces instead of surface tension over gravitational forces as in (2.2).

Performing a small-wavenumber expansion of the dispersion relation $D(k, \omega; Re, \cot\beta, We, Pr, Ma_{\Delta T}, B)$, similar to the one performed by Kalliadasis *et al.* (2003), leads to the following expression for the complex phase velocity:

$$c = 1 + \mathrm{i}k\left(\frac{2}{5}Re - \frac{1}{3}\cot\beta + \frac{Ma_{\Delta T}}{2(1+B)}\right) - \mathrm{i}k^3\frac{We}{3} + O(k^2) \tag{2.3}$$

where We is considered to be large such that $We\,k^2 = O(1)$. Note that the above expansion only gives the root of the dispersion relation that can become unstable. As was pointed out by Kalliadasis *et al.* (2003), the other two roots are always stable. The neutral stability condition is now easily found to be

$$c = 1, \quad k = \sqrt{\frac{1}{We}\left(\frac{6}{5}Re - \cot\beta + \frac{3Ma_{\Delta T}}{2(1+B)}\right)}. \tag{2.4}$$

Therefore, linear waves propagate with a velocity three times the averaged velocity or twice the interfacial velocity of the flat film. From (2.4) we also notice that increasing the Reynolds number or Marangoni number enlarges the range of unstable wavenumbers while decreasing β or increasing the Weber number has a stabilizing effect.

The onset of instability is obtained by considering the zero critical wavenumber as given by (2.4). This yields the critical condition

$$\frac{6}{5}Re + \frac{3Ma_{\Delta T}}{2(1+B)} = \cot\beta, \tag{2.5}$$

which is identical to the one obtained by Goussis & Kelly (1991) by performing a small wavenumber expansion of the Orr–Sommerfeld eigenvalue problem of the full Navier–Stokes/energy equations. The expression (2.5) has the same functional form as the one derived by Kalliadasis *et al.* (2003) for two-dimensional waves at criticality, but some of the coefficients are different: 6/5 instead of 1 in front of the Reynolds number, i.e. a 20% error, and 3/2 in front of the Marangoni number instead of 1/2 due to a factor of 3 introduced in the definition of the Marangoni number by Kalliadasis *et al.* (2003). Notice that here we try as much as possible to avoid numerical factors in the definitions of the dimensionless groups – with an exception to this rule being the definition of the Reynolds number – so that numerical factors in the equations do not change with different scalings. The discrepancy now for the coefficient in front of the Reynolds number corresponds exactly to the one observed using the Shkadov model (Shkadov 1967) in the case of an isothermal flow ($Ma_{\Delta T} = 0$). This inaccuracy has been eliminated by using a more complete description of the velocity field (Ruyer-Quil & Manneville 2000), which fully corrects the critical Reynolds number. Notice also that the Benney expansion for the heated falling film yields the correct critical Reynolds number (see Joo, Davis & Bankoff 1991). This is not surprising since this expansion is exact close to criticality (see our discussion in Part 1, § 1).

Let us now consider a falling film whose inclination angle, temperatures at the wall and air side and all physical quantities are fixed such that the sole control parameter is the liquid flux at the inlet or equivalently the Reynolds number $Re \propto \bar{h}_{\mathrm{N}}^3$. From (2.2), one has $Ma_{\Delta T} \propto 1/\bar{h}_{\mathrm{N}} \propto Re^{-1/3}$, $We \propto 1/\bar{h}_{\mathrm{N}}^2 \propto Re^{-2/3}$ and $B \propto Re^{1/3}$. Therefore, if the flow rate is large, inertia effects are large and the interfacial forces due to the Marangoni effects are not important compared to the dominant inertia forces, so that the H-mode dominates in this regime. Conversely, in the limit of vanishing Reynolds number, inertia effects are negligible and the Marangoni effect is very strong. This corresponds to the S-mode described by Scriven & Sternling (1964). In this region of small film thicknesses, the destabilizing forces are interfacial forces due to the Marangoni effect (capillary forces are always stabilizing). Since now $Ma_{\Delta T}/We \propto Re^{1/3}$, the critical wavenumber tends to zero as the Reynolds number tends to zero. This seems to contradict the results obtained by Goussis & Kelly (1991) which predict that the wavenumber approaches infinity in this limit. This inconsistency is due to the fact that Goussis & Kelly based the definition of their Marangoni number on the temperature difference across the basic flat film instead of the temperature difference between the wall and the ambient gas phase. As a consequence their Marangoni number should also depend on B (which in turn depends on Re) but this dependence was not taken into account in their study.

The Orr–Sommerfeld problem is a set of two complex ordinary differential equations of degree four and two, for the amplitudes of the perturbed cross-stream velocity and perturbed temperature, respectively, and subject to six boundary conditions. As these differential equations are linear, an integral constraint must be added, e.g. $\int_0^1 \phi(y)\,\mathrm{d}y = 1$ with $\phi(y)$ the amplitude of the perturbed cross-stream velocity. The Orr–Sommerfeld problem can then be recast in the form of a dynamical system of dimension six and subject to the above integral constraint. To solve numerically this

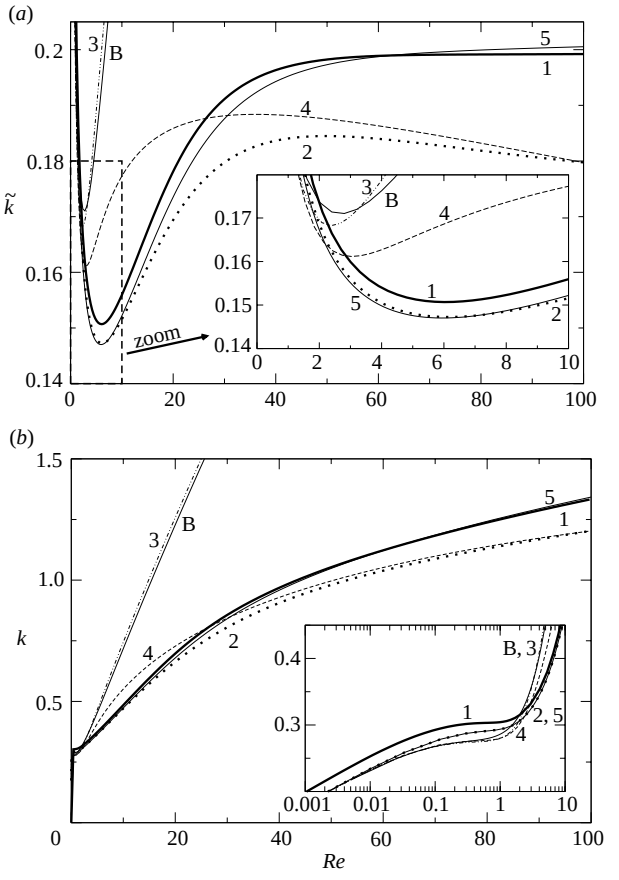

FIGURE 1. (*a*) Neutral stability curves in the $(\tilde{k}, Re)$-plane for $\Gamma = 250$, $\cot\beta = 0$, $Pr = 7$, $Ma = 50$ and $Bi = 1$ from the different models. (*b*) Neutral stability curves in the (k, Re)-plane; k is scaled with h_N. Thick solid curve 1: Orr–Sommerfeld; dotted curve 2: full-size second-order model; dot-dashed curve 3: first-order model; dashed curve 4: regularized reduced model (1.1); solid curve 5: boundary-layer equations. The solid curve B corresponds to the Benney long-wave expansion.

boundary-value problem, we utilized the long-wave nature of the instability. Indeed, the zero-wavenumber mode is neutral, i.e. $(\tilde{k},\ \tilde{\omega}) = (0,\ 0)$ is a solution of the eigenvalue problem. Therefore the solution branches were constructed by continuation starting from the trivial zero-wavenumber solution. For this purpose, we used the software AUTO97 developed by Doedel *et al.* (1997) and based on Keller's pseudo-arclength continuation method (Keller 1977). The same software was also used to obtain the dispersion relations of the other systems, namely, first-order, full-size second-order, boundary-layer and regularized reduced model.

In what follows, we fix the inclination angle β and all physical parameters – i.e. we fix the liquid–gas system or, equivalently, $\cot\beta$, Γ, Ma, Bi and Pr – as in a real experiment where the inlet flow rate is the actual control parameter. Therefore, we only vary the Nusselt film thickness h_N, or equivalently, the Reynolds number Re. Figure 1 depicts the neutral stability curves in the wavenumber–Reynolds number plane for $Pr = 7$, $\Gamma = 250$, $\cot\beta = 0$, $Ma = 50$ and $Bi = 1$ computed from the different models. The figure also shows the stability map obtained from the full Orr–Sommerfeld

stability analysis of the linearized Navier–Stokes/energy equations. The parameters are chosen so that the differences between the various systems of equations can be clearly identified. Hence the choice of an $O(1)$ and therefore unrealistically 'large' Biot number which would amplify the Marangoni effect. For the same reason, we choose to plot in figure 1(a) the critical wavenumber $\tilde{k}$ defined through the length-scale $\nu^{2/3}(g\sin\beta)^{-1/3}$ which only depends on the fluid parameters. Indeed as Re tends to zero, the prediction for the critical wavenumber k given in (2.4) tends to zero as $\sqrt{Ma_{\Delta T}/We}\propto\bar{h}_{\mathrm{N}}^{1/6}$. Thus $\tilde{k}=k/\bar{h}_{\mathrm{N}}\propto\bar{h}_{\mathrm{N}}^{-5/6}$ approaches infinity in that limit and the different curves are more easily separated.

The first-order model (curve 3) has already deviated from the other models at small Reynolds numbers. This is due to the relatively 'small' Kapitza number indicating that the second-order viscous effects are of primary importance in this regime. The full-size second-order model (curve 2) compares very well with the exact Orr–Sommerfeld solution (curve 1) even though at large Reynolds numbers it slightly underpredicts the neutral wavenumber. However, this small discrepancy at large Reynolds numbers cannot be attributed to the boundary-layer approximation (curve 5) since the trend is inverted in this latter case and it is most likely due to the limited radius of convergence of the perturbation scheme, as is the case with any approximate method. Nevertheless, we note the excellent agreement between the full-size model (curve 2) and the boundary layer equations (curve 5) for $Re<10$. Notice also the saturation of curves (1, 2, 5) for large Re: the critical wavelength $2\pi/\tilde{k}$ remains constant in this region and hence it is independent of the film thickness. On the other hand, at low Reynolds numbers all models are in agreement with the solution of the Orr–Sommerfeld eigenvalue problem. In this region, the dynamics of the flow is slaved to its kinematics, i.e. both flow rate and interfacial temperature are adiabatically slaved to the film thickness and they depend on time only through the dependence of the film thickness on time. This is the region where the Benney long-wave expansion applies.

Figure 1(b) depicts the marginal stability curves when the wavenumber is scaled with the base-state film thickness h_{N}. As expected, the curves approach the origin as Re decreases. Figure 3(a) in the study by Kalliadasis *et al.* (2003) on the other hand, indicates that for a vertically falling film with $Ma\neq0$ the neutral stability curves intersect the wavenumber axis at finite values. However, this was due to the relatively rough mesh in the computation of the neutral curves. A much smaller mesh shows that for Reynolds numbers smaller than $\sim10^{-4}$ (in terms of the scalings adopted by Kalliadasis *et al.* 2003) and for the parameter values used in the figure, the neutral curves turn sharply on themselves and approach the origin for very small Reynolds numbers as in figure 1(b). Finally, notice that all curves in figure 1(b) approach a plateau for $Re\sim1$.

By contrasting figures 1(a) and 1(b), it is evident that the principal advantage of the scaling based on the length scale constructed from the kinematic viscosity and gravitational acceleration, over the scaling based on the base-state film thickness, is to enable a clear distinction between the H- and S-modes of instability identified by Goussis & Kelly (1991). Indeed, the Orr–Sommerfeld neutral stability curve (curve 1) has a minimum at $R\approx5.6$ in figure 1(a). This minimum corresponds to the transition between the thermocapillary mode which predominates at low Reynolds numbers and the classical hydrodynamic mode which prevails at larger Reynolds numbers.

Figure 2 shows the growth rate $\mathrm{Im}\tilde{\omega}$ as function of $\tilde{k}$ for the long-wave instability of the basic flat-film solution. For the 'small' value $Re=1$, the growth rates predicted

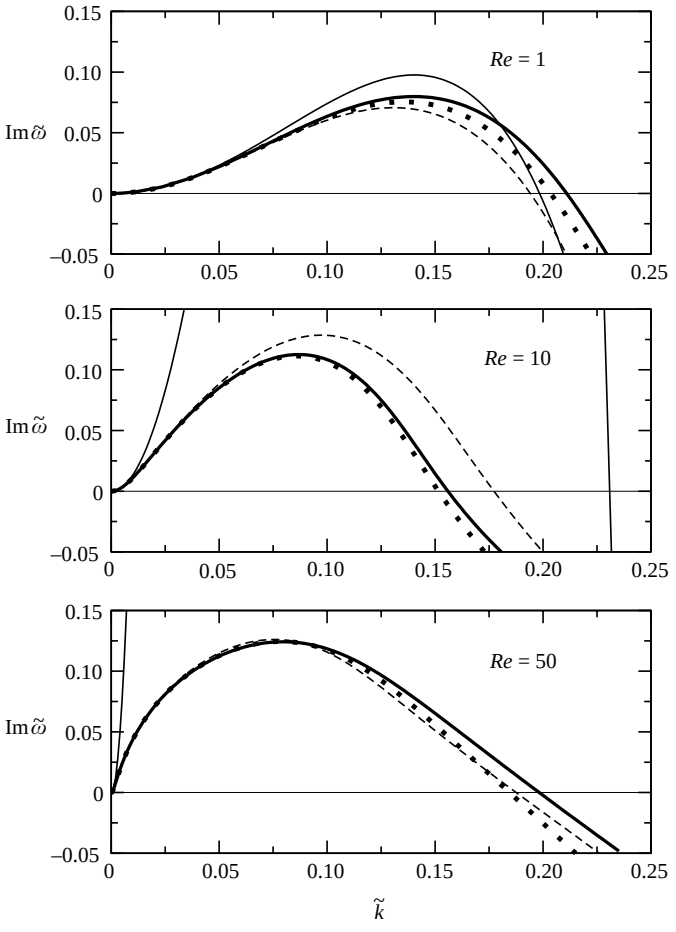

FIGURE 2. Growth rate $\mathrm{Im}\,\tilde{\omega}$ versus wavenumber $\tilde{k}$ for different Reynolds numbers obtained from the Orr–Sommerfeld analysis (solid lines), the full-size model (dotted lines), the regularized reduced model (dashed lines) and the Benney expansion (thin solid lines). Parameters are given in the caption of figure 1.

by the regularized reduced model (1.1), the full-size model and the second-order Benney expansion, are fairly close to the growth rate obtained by the exact Orr–Sommerfeld stability analysis. For larger Reynolds numbers, the Benney expansion no longer provides an accurate prediction for the growth rate, which increasingly deviates from the exact solution as the Reynolds number increases. This divergence is due to the fact that the Benney expansion assumes the dynamics of the flow to be slaved to its kinematics which is obviously not true at large Reynolds numbers. At $Re = 50$, where the H-mode is predominant, we note the good agreement of the full-size model and the regularized reduced model with the exact Orr–Sommerfeld analysis. At $Re = 10$, the full-size model is in good agreement with the exact Orr–Sommerfeld analysis while the regularized reduced model predicts a larger growth rate (still, the agreement with Orr–Sommerfeld is qualitative for all wavenumbers). This clearly shows the inability of the regularized reduced model to correctly take into account the second-order convective terms in the heat equation and to describe

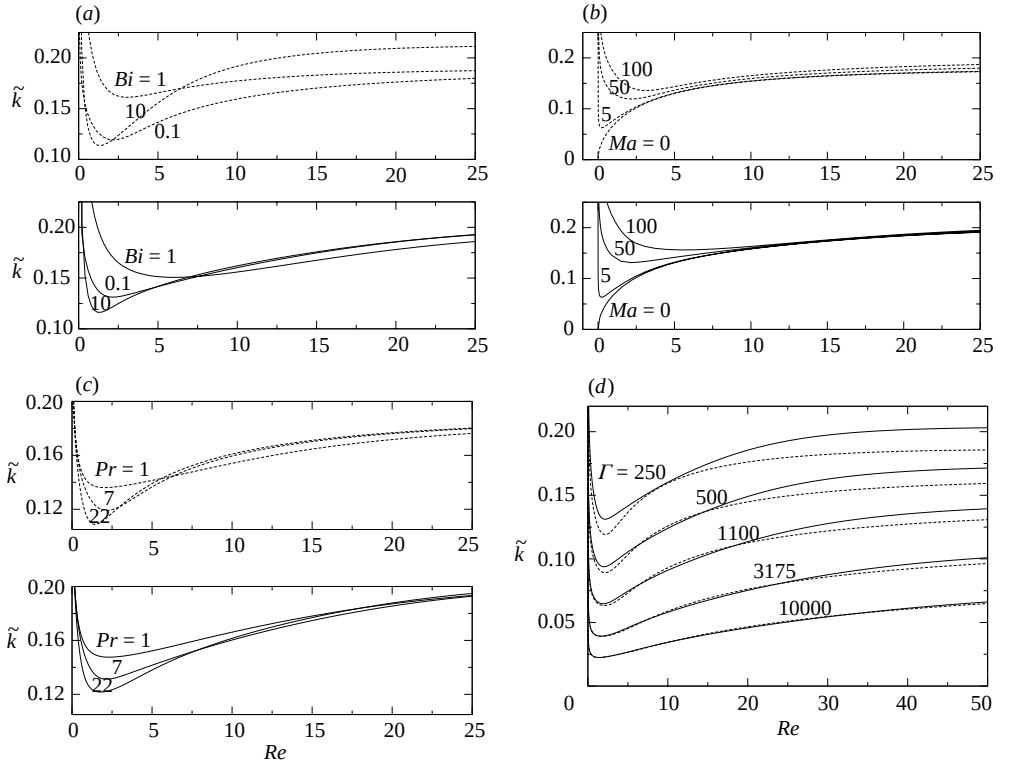

FIGURE 3. Influence of the Biot number (a), the Marangoni number (b), the Prandtl number (c) and the Kapitza number (d) on the marginal stability curves for a film falling down a vertical plane: (a) $Pr = 7$, $Ma = 50$ and $\Gamma = 250$; (b) $Bi = 0.1$, $Pr = 7$ and $\Gamma = 250$; (c) $Bi = 0.1$, $Ma = 50$ and $\Gamma = 250$; (d) $Bi = 0.1$, $Ma = 50$ and $Pr = 7$. The solid lines correspond to the Orr–Sommerfeld analysis and the dashed lines to the regularized reduced model (1.1).

the instability at large Péclet numbers where the S-mode is important. This issue will be discussed in the next section.

Figure 3(a) depicts the marginal stability curves obtained from the regularized reduced model (1.1) for a vertical plane and different Biot numbers. For $Bi = O(1)$ the influence of the Marangoni effect is large at small and moderate Reynolds numbers. Indeed, if Bi tends to zero or infinity, the free-surface temperature of the undisturbed solution, recalled in (2.1), becomes independent of h_N and the Marangoni effect is simply not an issue. For the other plots of figure 3, we choose a small Biot number, $Bi = 0.1$, which is motivated by experiments on the problem of a film heated by a local heat source (Kabov 1996; Kabov, Marchuk & Chupin 1996; Kabov *et al.* 2002) indicating that the Biot number in experiments is indeed small.

We have also investigated the influence of the Marangoni, Prandtl and Kapitza numbers and comparisons of the marginal stability curves obtained from Orr–Sommerfeld and the regularized reduced model are given in figure 3. As expected, for $Ma = 0$, we recover the classical hydrodynamic H-mode, with the corresponding curve starting from the origin of the plane ($\tilde{k}$, Re) – see figure 3(b). For $Pr = 7$, increasing the Marangoni number increases the range of unstable wavenumbers, especially at low Reynolds numbers where the Marangoni effect is predominant (S-mode). Again the results obtained using the regularized reduced model compare very well with the

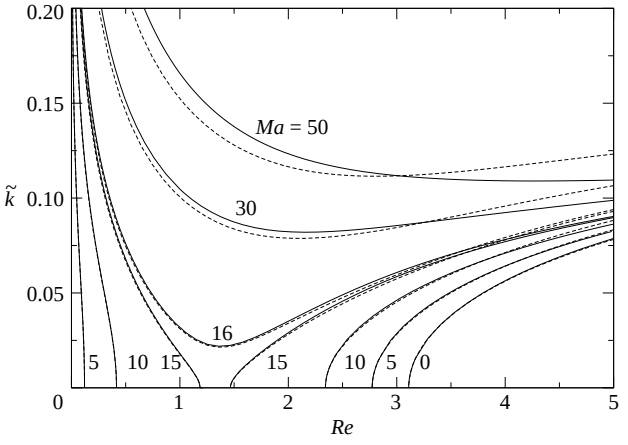

.

FIGURE 4. Influence of the Marangoni number on marginal stability for an inclined plane forming an angle $\beta = 15°$ with the horizontal direction with $\Gamma = 250$, $Pr = 7$ and $Bi = 1$. Solid lines are for the Orr–Sommerfeld analysis and dashed lines for the regularized reduced model.

Orr–Sommerfeld eigenvalue problem. Note, however, that at large Reynolds numbers, the marginal stability curves obtained from Orr–Sommerfeld merge into a single curve while the ones obtained from the regularized reduced model do not. Clearly, if Re is sufficiently large, the hydrodynamic H-mode predominates and the thermocapillary effects as measured by Ma do not modify significantly the critical wavenumber. The small disparity of the curves corresponding to the regularized reduced model is therefore a consequence of the increased inaccuracy of this model in the region of large Péclet numbers.

Figure 3(c) depicts the effect of Prandtl number on the marginal stability curves. The results now are less intuitive. Indeed, since the instability is primarily an inertia-driven instability, at least if the H-mode predominates, a larger value of Pr would imply a larger range of unstable wavenumbers since the Péclet number, $Pe = PrRe$, measuring the convective effects in the heat transport equation is also larger. Nevertheless, it is found that the Prandtl number has little influence for large Re (H-mode) whereas the curves are strongly affected by the Prandtl number for small Re (S-mode). If the S-mode predominates, the origin of the instability is the gradient of temperature at the interface. This gradient may be weakened by the transport of heat from the troughs to the crests due to the motion of the fluid, a process which is intensified with large Prandtl numbers. Note that the regularized reduced model agrees better with Orr–Sommerfeld for $Pr = 1$ than for larger values of Pr.

Finally, figure 3(d) shows the influence of Kapitza number on the marginal stability curves. Note the excellent agreement with the Orr–Sommerfeld eigenvalue problem for large values of Γ ($\Gamma = 3175$ corresponds to water at 18 °C). Now, decreasing the value of Γ increases the range of unstable wavenumbers and a discrepancy between the regularized reduced model and the Orr–Sommerfeld eigenvalue problem appears, which increases with decreasing Γ. It is precisely for this reason, i.e. to emphasize the differences between the different models, that we choose the worse case scenario in which the Kapitza number is relatively small, $\Gamma = 250$, throughout this study.

For non-vertical planes and Marangoni numbers Ma of $O(1)$, the critical condition (2.5) can lead to two different values for the onset of the instability corresponding to

the H- and S-modes, respectively. This is confirmed in figure 4 for a plane inclined at an angle $\beta = 15^\circ$ with respect to the horizontal direction. For moderate values of *Ma*, two distinct unstable regions are observed, each corresponding to a different instability mode as reported first by Goussis & Kelly (1991). Note the excellent agreement of the curves corresponding to the regularized reduced model (1.1) with Orr–Sommerfeld in the vicinity of the two thresholds. This agreement results from taking into account the second-order dissipative terms in our formulation and from a correct representation of the instability threshold. Noticeable discrepancies between the two sets of curves can be observed if the Marangoni number is increased or at larger Reynolds numbers. Finally, we have analysed the linear stability properties of different second-order reduced models, but in all cases, the system in (1.1) offers the best agreement with Orr–Sommerfeld.

3. Solitary waves

We now seek travelling wave solutions of (1.1). Here we restrict our attention to single-hump solitary waves. It is well known that for isothermal films, the long-time evolution is characterized by a train of soliton-like coherent structures each of which resembles the infinite-domain solitary pulses (see e.g. Alekseenko, Nakoryakov & Pokusaev 1994). Although time-dependent computations are beyond the scope of the present study, by analogy with the isothermal case, we anticipate that for the non-isothermal problem studied here, the long-time evolution is also dominated by solitary waves.

Comparisons of the different shapes of solitary waves is made easier by using a scaling based on the intrinsic length scales of the structures considered. For this purpose we adopt the scalings suggested by Shkadov (1977). These scalings are motivated by the observation that the largest slope of a solitary wave is at the front of the main solitary hump where the breaking of the wave is promoted by the stream wise gravity force $\rho g \sin\beta$ and balanced by the pressure gradient induced by the surface tension $\propto \sigma \partial_{xxx} h$. Therefore the characteristic slope $1/\kappa$ is given by $(\rho g h_{\mathrm{N}}^2 \sin\beta/\sigma)^{1/3} = We^{-1/3}$. This analysis is valid at least close to the threshold of instability where the range of unstable wavenumbers is small. Thus introducing the transformation $x \to \kappa \bar{h}_{\mathrm{N}} x$, $y \to \bar{h}_{\mathrm{N}} y$, $u \to \bar{h}_{\mathrm{N}}^2 u$, $t \to t\kappa/\bar{h}_{\mathrm{N}}$ in the boundary-layer equations (see § 3 in Part 1) yields

$$\delta(\partial_t u + u\partial_x u + v\partial_y u) - (\partial_{yy} + 2\eta\partial_{xx})u - \eta\partial_x[\partial_x u|_h] - 1 + \zeta\partial_x h - \partial_{xxx} h = 0, \quad (3.1a)$$

$$Pr\delta\left(\partial_t T + u\partial_x T + v\partial_y T\right) - (\eta\partial_{xx} + \partial_{yy})T = 0, \quad (3.1b)$$

completed by the continuity equation $\partial_x u + \partial_y v = 0$, the boundary conditions

$$\partial_y u|_h = \eta(4\partial_x h\partial_x u|_h - \partial_x v|_h) - M\partial_x[T|_h], \quad (3.2a)$$

$$\partial_y T|_h = -B\left(1 + \frac{\eta}{2}(\partial_x h)^2\right)T|_h + \eta\partial_x h\partial_x T|_h, \quad (3.2b)$$

the kinematic condition at the free surface $\partial_t h + u|_h \partial_x h = 0$ and the Dirichlet conditions at the wall, $u|_0 = v|_0 = 0$ and $T|_0 = 1$. A set of 'reduced' parameters is now obtained:

$$\left.\begin{aligned} \delta &= \frac{\bar{h}_{\mathrm{N}}^3}{\kappa} = \frac{(3Re)^{11/9}}{\Gamma^{1/3}}, \quad \zeta = \frac{\cot\beta}{\kappa} = \frac{\cot\beta\,(3Re)^{2/9}}{\Gamma^{1/3}}, \\ \eta &= \frac{1}{\kappa^2} = \frac{(3Re)^{4/9}}{\Gamma^{2/3}}, \quad M = \frac{Ma}{\kappa\bar{h}_{\mathrm{N}}^2} = \frac{Ma}{\Gamma^{1/3}(3Re)^{4/9}}, \end{aligned}\right\} \quad (3.3)$$

along with $B = Bi\,(3Re)^{1/3}$ defined in (2.2); δ is the reduced Reynolds number† and ζ the reduced slope. The parameter η appears in all second-order streamwise dissipative terms in the momentum and heat transport equations. Similarly M is a reduced Marangoni number. Since the long-wave approximation requires the slope to be small, η must be small – or equivalently the Kapitza number large enough – so that in many studies dealing with vertical isothermal film flows ($\zeta = 0$, $M = 0$) η is set to zero and the set of parameters is reduced to δ only (see e.g. Chang 1994). Again, considering isothermal vertical flows, another advantage of the above set of parameters is that, using Shkadov's scalings, the speed and maximal height of the solitary waves depend strongly on the reduced Reynolds number δ and are not affected much by the strength of the streamwise viscous terms as measured by η, whereas the amplitude of the front-running capillary waves depends strongly on η (see e.g. the direct numerical computations by Salamon, Armstrong & Brown 1994). Still considering isothermal vertical flows, if the effect of inertia becomes dominant, the maximum slope of the waves ceases to correspond to the equilibrium of the streamwise gravity and surface tension but rather to the largest wavenumber triggered by the instability which corresponds to the critical wavenumber $k_c \propto \sqrt{Re/We}$ (see (2.4)). Therefore $\epsilon Re \sim k_c Re \sim \delta^{3/2}$ and the transition from the drag–gravity regime ($\epsilon Re \ll 1$) to the drag–inertia regime ($\epsilon Re = O(1)$) corresponds to δ of order unity. As already noticed by Ooshida (1999), this transition corresponds closely to the loss of solitary wave solutions observed for the Benney equation for $\delta \approx 0.986$. Finally, the reduced parameters (3.3) also give a good indication of the influence of the different physical effects on these waves. Therefore, since Shkadov's scalings are appropriate for the study of the strongly nonlinear solitary waves, in the next section we shall compare the main properties of the solutions obtained from the regularized reduced model – namely phase speed c, maximum height and shapes – using these scalings also.

Interestingly, all the reduced parameters (3.3) vanish as the Reynolds number tends to zero except for the reduced Marangoni number which tends to infinity. Hence, for small flow rates, $\delta \ll 1$, $\zeta \ll 1$ and $\eta \ll 1$ and the corresponding terms multiplied by these parameters can be neglected. Integrating (3.1) twice thus leads to

$$q = \frac{h^3}{3}(1 + \partial_{xxx}h) - \frac{M}{2}h^2\partial_x\theta, \quad \theta = \frac{1}{1+Bh} = 1 - Bh + O(B^2), \tag{3.4}$$

and the mass conservation equation $\partial_t h + \partial_x q = 0$ then gives

$$\partial_t h + \partial_x \left[\frac{h^3}{3}(1 + \partial_{xxx}h) + \frac{MB}{2}h^2\partial_x h\right] = 0 \tag{3.5}$$

where the leading-order term involving B has been retained. Apart from numerical factors and different scalings, equation (3.5) is identical to the one obtained by Kalliadasis *et al.* (2003). The reduced parameter proposed by Kalliadasis *et al.* (2003) is $\propto 1/BM$. These authors observed that homoclinic solutions to (3.5) tend to infinity as their parameter tends to zero, that is when MB tends to infinity. Because we have $MB \propto (3Re)^{-1/9}$, this limit corresponds to the zero Reynolds number limit. As was pointed out by these authors, in this region of small flow rates and hence small film thicknesses, the film is expected to form isolated drops separated by very thin

† The reduced Reynolds number defined initially by Shkadov (1977) was $\delta_{\mathrm{Shk}} = \delta/45$. The numerical factor originates from a slightly different choice of variables.

layers of fluid for which van der Waals forces become important. Such forces of non-hydrodynamic origin are expected to arrest the singularity formation observed for the homoclinic orbits in the region of small Reynolds numbers. Inversely, if Re tends to infinity, both M and MB tend to zero and the velocity and temperature fields are decoupled in this limit. Therefore, at large Reynolds numbers, the shape of the wave should be unaffected by the Marangoni effects. These two limits will enable us to elucidate the influence of Reynolds number on the shape of the waves for given inclination angle and physical properties.

In what follows, we discuss in detail the properties of the solitary wave solutions of the system (1.1) as well as the influence of the different physical effects and different parameters, primarily Re, Pr and Ma, on these waves. In all cases the wall is taken to be vertical – for the isothermal case vertical apparatus is most frequently used in experiments (Alekseenko, Nakoryakov & Pokusaev 1994). Our main interest is to decipher the coupling between the hydrodynamic H-mode and thermocapillary S-mode in the nonlinear regime and particularly for large amplitude waves, that is in the drag–inertia regime where inertia plays a dominant role.

Consider now travelling wave solutions propagating at constant speed c and hence stationary in the moving frame $\xi = x - ct$. In this frame, the set of equations (1.1) can be written in dynamical system form as

$$\frac{\mathrm{d}\boldsymbol{U}}{\mathrm{d}\xi} = \boldsymbol{F}(\boldsymbol{U};\, \delta,\, \zeta,\, \eta,\, B,\, M,\, Q), \tag{3.6}$$

where $\boldsymbol{U} = (h,\, h',\, h'',\, \theta,\, \theta')^t$. The constant Q is the mass flux under the wave in the moving frame of reference and is obtained after one integration of the mass conservation equation $-c\,h' + q' = 0$, $Q = q - c\,h$. For solitary pulses, the Nusselt flat-film solution $h = 1$ should be approached far from the pulses which gives $Q = 1/3 - c$. Since the speed of the waves is larger than the maximum velocity in the liquid, Q is a negative constant. Note, however, that in experiments, the time-averaged film thickness can be smaller downstream than at the inlet (the presence of the waves usually accelerates the fluid motion). As a consequence, the local Reynolds number varying with the third power of the thickness can be significantly smaller than the Reynolds number based on the flow rate or the inlet Nusselt film thickness.

Singe-hump solitary wave solutions – also called 'principal homoclinic orbits' by Gelndinning & Sparrow (1984) – are computed using the continuation software AUTO97 with the HOMCONT option for tracing homoclinic orbits (Doedel *et al.* 1997). In figure 5 we present the maximum amplitude and speed of the single-hump solitary wave family of the regularized reduced model as a function of Re for different values of Prandtl and Marangoni numbers. For comparison purposes, we also show in the same figure the wave family corresponding to isothermal flows ($Ma = 0$). In all our computations in this section we take the values $\Gamma = 250$ and $Bi = 0.1$ for the Kapitza and Biot numbers, respectively. As already mentioned, the Kapitza number is chosen much smaller than its value for common liquids in order to clearly isolate the role of the second-order dissipative and inertia terms.

The single-hump solitary wave solution branch obtained from (1.1) seems to exist for all Reynolds numbers, i.e. it does not present any turning points with branch multiplicity connected to finite-time blow-up behaviour as for the Benney expansion (Pumir, Manneville & Pomeau 1983; Oron & Gottlieb 2002; Scheid *et al.* 2005). Different reduced second-order formulations – from the family of reduced models developed in Part 1 – were also tested (not shown) and their solitary-wave solution branches do exhibit turning points. This, along with the good agreement with the

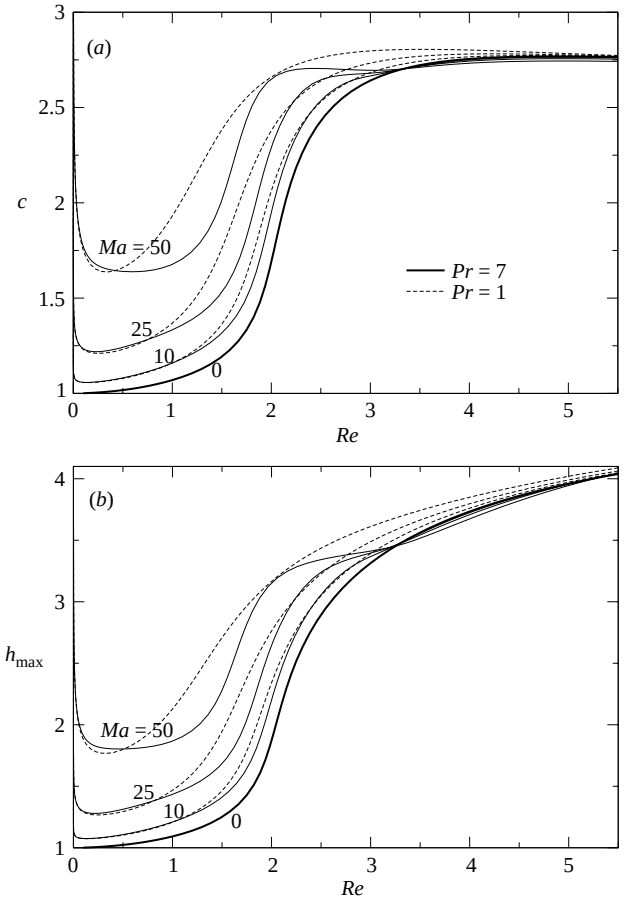

FIGURE 5. (*a*) Speed and (*b*) maximum height of single-hump solitary wave solutions computed with the regularized reduced model (1.1) for different values of Ma and Pr with $\cot\beta = 0$, $Bi = 0.1$ and $\Gamma = 250$.

Orr–Sommerfeld eigenvalue problem shown in the previous section, confirms that (1.1) is indeed a well-behaved low-dimensional model.

As expected, increasing the Marangoni number leads to larger amplitudes and speeds since the two instability modes reinforce each other. This effect is more pronounced at low Reynolds numbers (the reduced Marangoni number M defined in (3.3) is proportional to $Re^{-4/9}$). This is also consistent with our linear stability analysis in the previous section which suggests that the Marangoni effect is amplified in the region of small Reynolds numbers. On the other hand, in the region of large Re, the different curves merge with the isothermal one. In this region of large Reynolds numbers the destabilizing interfacial Marangoni forces are weaker than the dominant inertia forces.

The effect of Prandtl number is more subtle. At low Reynolds numbers, larger values of Pr seem to favour the instability, whereas at larger Re, we have the opposite effect. To elucidate the influence of Prandtl number, we compute the streamlines and isotherms in the moving frame by computing the velocity and temperature fields from the polynomial expansions and by utilizing the first-order approximation of the corrections s_i and t_i (see Part 1 for details). Note that the second-order corrections for

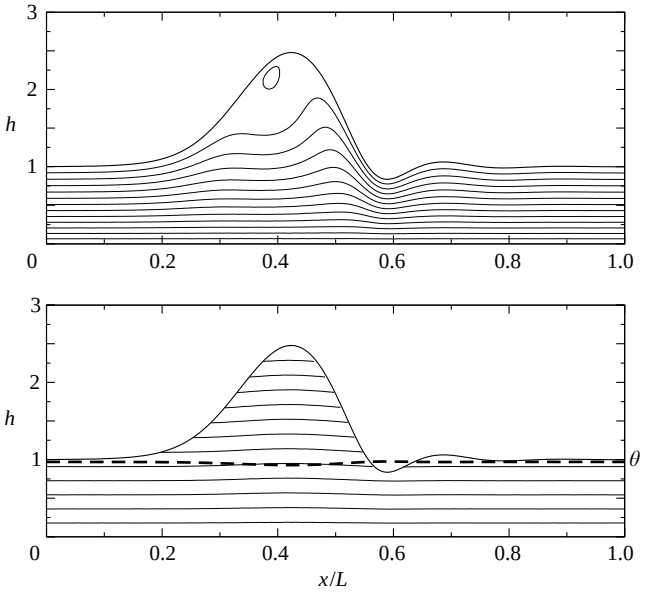

FIGURE 6. Streamlines (top) and isotherms (bottom) of a solitary wave in its moving frame obtained for $Pr = 7$, $Re = 0.01$, $\cot\beta = 0$, $\Gamma = 250$, $Ma = 50$ and $Bi = 0.1$. The dashed line represents the interfacial temperature θ. There are 12 isotherms separating 13 equally spaced intervals, ranging from $T = 1$ on the wall to $T_{\min} = 0.929$.

both fields can also be computed from the residuals associated with the corresponding test functions followed by an inversion of the resulting linear system. Nevertheless, due to the complexity of this procedure, we assume here that the velocity and temperature fields are described sufficiently accurately by their representation at first order, at least for the purpose of a qualitative discussion. In all computations of this section the Marangoni number is fixed at $Ma = 50$.

Figure 6 shows the streamlines and isotherms for $Re = 0.01$. The reduced parameters are $\delta = 0.0022$, $\eta = 0.0053$, $M = 37.6$ and $B = 0.031$. With the product $Pr\delta$, η and B being small, the film flow evolution is well approximated by the evolution equation for the free surface (3.5). We also have $\partial_{yy}T \approx 0$ so that the temperature field is nearly linear, $T \approx 1 - By$. Therefore, the isotherms are nearly aligned with the wall. Notice also from figure 6 that the interfacial temperature θ is nearly uniform since $B \ll 1$. For such a small Reynolds number, inertial effects are almost absent and the Marangoni effect is free to form large-amplitude humps. Consequently, the phase speed is sufficiently large – $c = 2.35$ for the wave shown in figure 6 – to create a recirculation zone at the crest of the wave along with the transport of fluid mass downstream. Interestingly, this behaviour triggered by the Marangoni effect is very similar to that triggered by inertia for larger Reynolds numbers (see below).

The streamlines and isotherms computed for $Re = 1$ and $Pr = 1$ and 7 are shown in figure 7. The reduced parameters are now $\delta = 0.61$, $\eta = 0.041$, $M = 4.86$ and $B = 0.14$. Again, at $Pr = 1$, the isotherms are nearly aligned (with both B and $Pr\delta$ being still relatively small). Conversely, at $Pr = 7$, the isotherms are deflected upwards by the movement of the fluid in the crest. Therefore, the minimum of temperature (which is achieved at the crest of the solitary wave) increases to $T_{\min} = 0.8$ – from 0.765 for $Pr = 1$ – and consequently the Marangoni effect is reduced, and therefore the amplitude and the phase speed of the wave are also reduced. The transport of heat

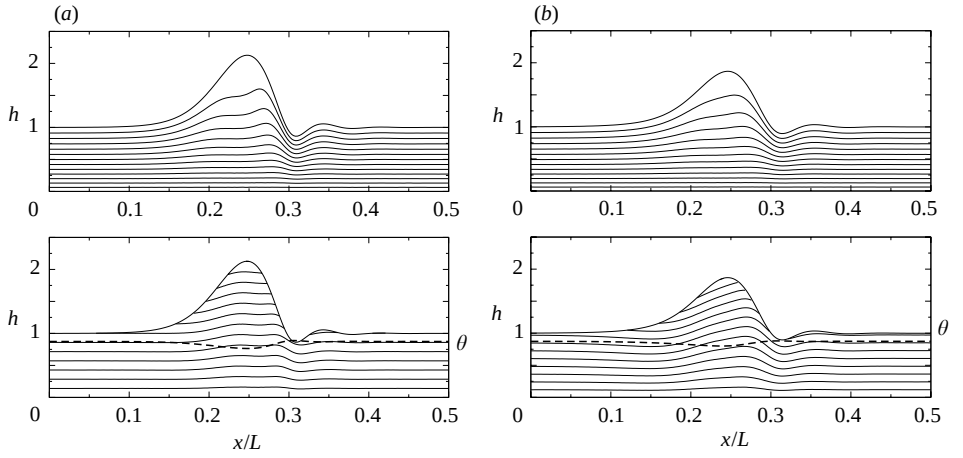

FIGURE 7. Streamlines (top) and isotherms (bottom). $Re = 1$ and all other parameters are given in the caption of figure 6. In (*a*) $Pr = 1$ and $T_{\min} = 0.765$ and in (*b*) $Pr = 7$ and $T_{\min} = 0.8$. In all cases, a total of 12 isotherms separating 13 equally spaced intervals between $T = 1$ and $T = T_{\min}$ is shown.

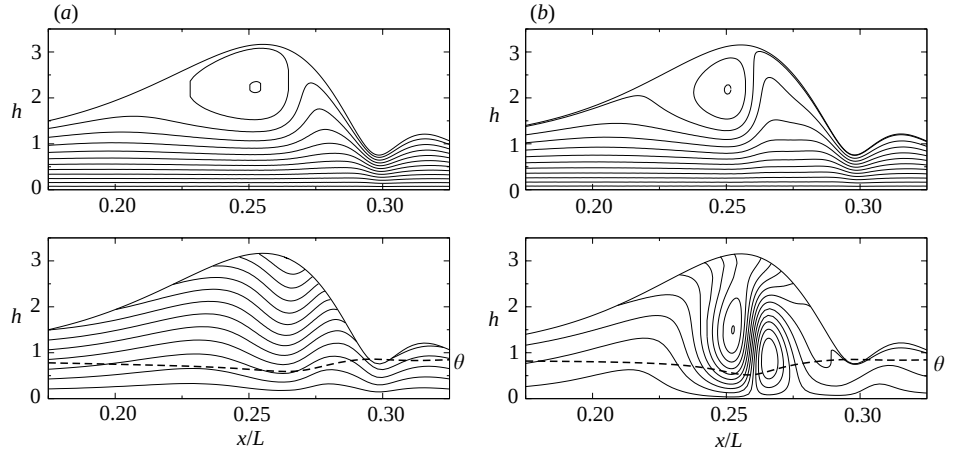

FIGURE 8. Streamlines (top) and isotherms (bottom) for $Re = 2$. All other parameters are given in the caption of figure 6. In (*a*), $Pr = 1$ and $T_{\min} = 0.591$ and in (*b*), $Pr = 7$, $T_{\min} = 0.429$ and $T_{\max} = 1.26$.

by the motion of the fluid has a stabilizing effect in this case. Nevertheless, at larger Reynolds numbers, inertia dominates, the solitary wave amplitude and speed increase dramatically and a recirculation zone appears inside the solitary wave. Streamlines computed for $Re = 2$ and $Re = 3$ ($\delta = 1.42$ and $\delta = 2.33$) shown in figures 8 and 9 do exhibit such recirculation zones, turning clockwise, and implying the existence of two stagnation points at the free surface at the back and the front of the primary solitary hump. In this case solitary waves transport the trapped fluid mass downstream.

Comparison with the streamlines at $Re = 3$ when the thermocapillary effect is switched off ($Ma = 0$) indicate that the Marangoni instability shifts one of the stagnation points from the front of the wave to its crest (see figure 10). Thus, because thermocapillary stresses push the fluid from the rear to the top of the crest,

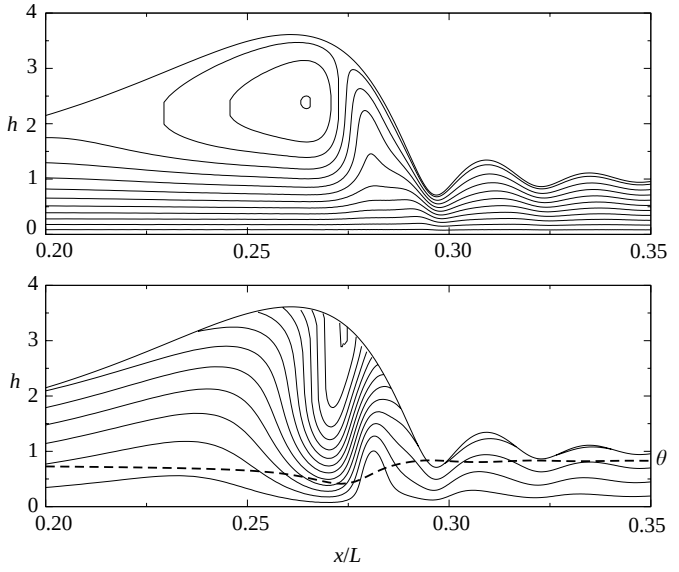

FIGURE 9. Streamlines (top) and isotherms (bottom) for $Re = 3$ and $Pr = 1$. Here $T_{\min} = 0.414$.

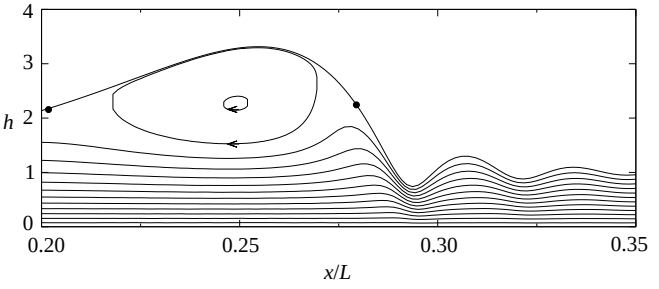

FIGURE 10. Streamlines for $Ma = 0$, $Re = 3$, $\cot\beta = 0$ and $\Gamma = 250$.

they reinforce the clockwise circulation in the crest. Meanwhile, the transport of heat by the downward fluid motion at the front of the recirculation zone cools down the surface at its crest and the minimum of interfacial temperature is now located close to the stagnation point at the front. Therefore the two mechanisms reinforce each other, promoting the speed and amplitude of the wave. This explains the formation of a recirculation zone at $Re = 2$ and $Ma = 50$ whereas it is not present if $Ma = 0$. Indeed, the abrupt increase of amplitude and speed of the solitary waves corresponding to the transition from the drag–gravity to the drag–inertia regime occurs for smaller values of the Reynolds number if the Marangoni effect is present (see figure 5).

Comparison of figures 8(a) and 8(b) indicates that increasing the Prandtl number from $Pr = 1$ to $Pr = 7$ at $Re = 2$ enhances the cooling process of the crest and reduces the temperature minimum from $T_{\min} \equiv \theta_{\min} = 0.591$ – which appears on the surface and very close to the stagnation point – to $T_{\min} = 0.429$ somewhere in the bulk of the wave, thus contributing to the Marangoni effect. Similarly, comparing figures 8(a) and 9, $T_{\min} \equiv \theta_{\min}$ drops from to 0.591 to 0.414 when Re increases from 2 to 3 at $Pr = 1$.

However, if the H- and S- instability modes reinforce each other for $Re = 2$ and $Re = 3$, the speed and amplitudes of the solitary waves do decrease as the Prandtl number increases as indicated in figure 5. This apparent paradox can be explained only by observing that on shifting one of the stagnation points to the crest, thermocapillarity tightens the streamlines and isotherms at the front of the recirculation zone. Moreover, the circulation in the hump is enhanced by the Marangoni stresses at the surface. Therefore, large temperature and velocity gradients appear in that region of the flow. As a consequence, the dissipation of heat and momentum is increased, which contributes to stabilizing the growth of the instability and to limiting the speed and amplitude of the solitary waves.

For $R = 2$ and $Pr = 7$, the maximum of temperature is $T_{\max} = 1.216$ and is no longer located at the wall. Notice also that at larger values of the Reynolds number, negative values of the dimensionless temperature appear in the fluid. Turning back to dimensional quantities, this would imply that the temperature in the fluid can be locally greater than the temperature of the wall or smaller than the temperature of the air. This obviously has no physical basis as the temperature everywhere in the fluid should be bounded between the wall and air temperatures. To understand the appearance of this unphysical behaviour when a recirculation zone is present, i.e. for large-amplitude waves, let us consider the high-Péclet-number limit $Pe = PrRe \gg 1$. In this case, transport of heat via molecular diffusion can be neglected except in a diffusive boundary layer of thickness $Pe^{-1/2}$ on the stagnation line and part of the interface associated with the recirculation zone (see e.g. discussion by Shraiman 1987). Hence, cross-stream convection associated with the recirculation zone dominates over diffusion, the temperature field in the recirculation zone is simply transported by the flow and the streamlines are identical to the temperature contours (see e.g. Trevelyan *et al.* 2002). This means that the temperature along each streamline is constant due to the strong advection mixing. The temperature field becomes a passive scalar and is simply transported by the flow. Hence, within the recirculation zone the isotherms are closed curves. Consequently, the temperature can vary locally in the horizontal direction only and the hypothesis $\partial_y T \gg \partial_x T$ necessary for the derivation of our models would be violated in these regions.†

At the same time we have neglected in the averaged heat balance (1.1*c*) the transport of heat due to the Marangoni flow, Mar_θ (see § 5 in Part 1). Though these terms are formally of second order, they could be quite significant due to the enhancement of the Marangoni flow by the hydrodynamics. This might also contribute to the appearance of negative temperatures. Different possibilities – not examined here – exist to cure this strong limitation on the applicability of the three-equation model (1.1). One such possibility would be to consider more unknowns, such as t_1, for the description of the heat transfer process in the flow. Another possibility would be to relax the assumption $\partial_y T \gg \partial_x T$ and use instead the full energy equation without any approximations. In this case the full energy equation would have to be solved numerically to obtain the temperature distribution within the film.

The basic question here is whether the observed limitations are truly due to a breakdown of the basic assumptions at large Péclet numbers and for large-amplitude waves for which recirculation zones could be observed, or are spuriously caused by the addition of the strongly nonlinear second-order terms appearing in the expansion

† Note however that the presence of recirculation zones does not invalidate the assumption $u \gg v$ necessary for any boundary-layer approach since the computed streamlines correspond to the envelopes of the velocity field in the moving frame $(u - c,\ v)^t$.

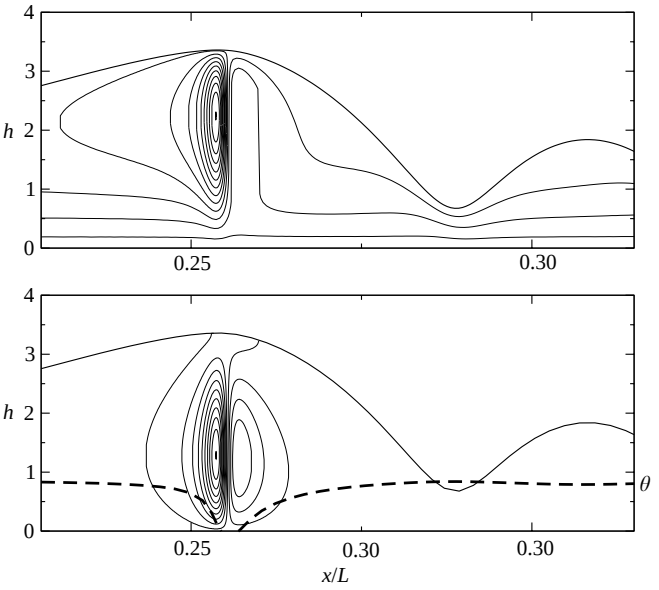

FIGURE 11. Streamlines (top) and isotherms (bottom) for $Re = 2.5$ and $Pr = 7$ obtained from the first-order model. Here $T_{\min} = -10$ and $T_{\max} = 4$.

procedure. To check these possibilities, we have computed the single-hump solitary wave solution branch corresponding to the first-order model (system (4.18) in Part 1) for $\Gamma = 250$, $\cot\beta = 0$, $Bi = 0.1$ and two values of the Prandtl number, $Pr = 1$ and $Pr = 7$. In both cases, a limit point, at which the branch of solutions terminates, appears (at $Re \approx 2.4$ for $Pr = 1$ and $Re \approx 2.7$ for $Pr = 7$). This loss of solutions follows the formation of steep temperature gradients in the bulk of the flow as is evident from the isotherms shown in figure 11 at $Re = 2.5$ and $Pr = 7$. In fact, the isothermal first-order model, an improved representation of the Shkadov model, has no limit points and so the limit points for the non-isothermal model must be due to the treatment of the energy equation. Notice that, quite surprisingly, the loss of solutions appears at smaller values of Re for $Pr = 1$ than for $Pr = 7$. This unusual result can be attributed to the fact that the transition between the drag–gravity and the drag–inertia regimes is delayed by the upward displacement of the isotherms by the flow as already observed in figure 7. Consequently, the second-order terms do contribute to the delay of the breakdown of our formulation and hence the limitations of our model are not caused by the added second-order terms. This effect is certainly due to the fact that the second-order diffusion terms reduce the range of unstable wavenumbers and smooth out temperature gradients (compare the amplitude of the front-running capillary wave preceding the main hump in figures 9 and 11).

It is important to emphasize that unlike the first-order model, the second-order regularized reduced model has no limit points at which the solution branches terminate. This is due to an improved treatment of the energy equation by taking into account the second-order dissipative terms in the streamwise direction as mentioned above. The first-order model on the other hand has not taken into account these terms – contrast (1.1c) with (4.18c) of Part 1. It is precisely the presence of diffusion of heat in the streamwise direction for the regularized reduced model that smooths out the large temperature gradients as was pointed out above and hence this model has no limit points. Nevertheless, for sufficiently large Péclet numbers and as we

have already pointed out, negative temperatures are observed somewhere in the bulk of the wave. The *Re* value at which this happens depends on *Pr*, with the larger *Pr* corresponding to smaller *Re* at which negative temperatures appear. After these points, the bifurcation diagrams for the speed of the solitary waves c as a function of *Re* can be continued to larger *Re* but the temperature will remain negative (in fact continuation of the curves in figure 5 will eventually lead to negative temperatures). The reason that this continuation is possible is that c is effectively determined by the momentum equation which is treated accurately; it is the treatment of the energy equation that needs to be improved and some suggestions for this have already been discussed above.

4. Concluding remarks

We have analysed the linear and nonlinear regimes of the two long-wave instability modes for a film falling down a uniformly heated plane by using the regularized reduced model derived in Part 1. The linear stability properties of the model are in good agreement with the Orr–Sommerfeld analysis for small and moderate Reynolds numbers and for all Marangoni numbers (§ 2) while its single-hump solitary wave solution branches do not exhibit the non-physical turning points encountered with the Benney equation (§ 3). Therefore, time-dependent integrations of the regularized reduced model (1.1) (not done here) should not lead to the finite-time blow-up behaviour observed with the Benney expansion in the region of the parameter space where solitary waves do not exist.

We also examined in detail the shape, streamlines and isotherms of single-hump solitary waves obtained from the regularized reduced model and for different Reynolds, Prandtl and Marangoni numbers. In the drag–gravity regime, the transport of energy by the flow contributes to heating the crest of the solitary waves. In this region, the inertial terms in the averaged heat transport equation have a stabilizing effect. For $Re \ll 1$, inertial effects are nearly absent and the Marangoni effect is free to form large-amplitude humps and hence large phase speed so that a recirculation zone at the crest of the wave appears. As far as we are aware, a recirculation zone has never been obtained before for such small Reynolds numbers and is usually known to exist only in the drag–inertia regime for large Reynolds numbers. In this regime, the amplitudes and speeds of the solitary waves are also large. However, the effect of the transport of heat by the flow is reversed. One of the stagnation points (in the frame moving with the wave) is shifted from the front of the wave to its crest. Thus, the Marangoni effect enhances the recirculation in the crest and promotes a strong downward flow there. As a consequence, the transport of heat by the flow contributes to cooling the crest and amplifying the Marangoni effect. Nevertheless, this strong circulation and downward flow create a strong shear and therefore increase the effect of viscous dissipation which in turn reduces the amplitude and speed of the waves if the Prandtl number increases. These observations indicate that the interaction of the hydrodynamic H-mode and the Marangoni S-mode is non-trivial especially in the region of large-amplitude solitary waves.

With regard to experiments, comparisons with the theory developed here should be facilitated by the fact that most fluids used in applications have high Kapitza numbers. Note also that the heat transfer coefficient is generally small so that the Biot number is also small. Thus considering the limit $Bi \ll 1$, the basic-state temperature gradient $b_\perp = (T|_{y=0} - T|_{y=h_N})/h_N = Bi/(1 + Bih_N)$ can be assumed to be independent of the film thickness h, $b_\perp \approx Bi$. This basic-state temperature gradient is then uniquely

defined by the heat transfer coefficient q_0 and the diffusivity κ and not by the flow rate. As a consequence, many studies on Marangoni instabilities have used explicitly the gradient $b_\perp$ to scale the temperature field (Takashima 1981; Davis 1987; Goussis & Kelly 1991). Following this approach, one can define a reference temperature T_{s0} corresponding to the surface temperature of a flat film of thickness equal to the length scale $\nu^{2/3}(g\sin\beta)^{-1/3}$. A new dimensionless temperature $T^\star$ is thus introduced using the difference $T_w - T_{s0}$ such that $T^\star = 1$ at the wall and $T^\star = 0$ at the surface of the film of thickness l_0. T and $T^\star$ are then related by

$$T = \frac{1 + BiT^\star}{1 + Bi}, \tag{4.1}$$

and the heat transfer condition at the interface becomes

$$-\nabla T^\star \cdot \boldsymbol{n} = BiT^\star + 1. \tag{4.2}$$

The linear stability analysis of a thin film in the limit of a vanishing Biot number was considered by Takashima (1981). Obviously, taking this limit is not consistent with the problem in hand as $Bi = 0$ implies that the transfer of heat through the fluid layer vanishes and therefore the temperature at the free surface is constant. Nevertheless, the product $Ma\,Bi$ can be $O(1)$ even if Bi is small and so the Marangoni effect can be strong. Thus, Takashima's limit corresponds in fact to a constant temperature gradient $q_0(T_w - T_a)/\kappa$, that is simply obtained by neglecting the term $BiT^\star$ in (4.2) which gives

$$\nabla T^\star \cdot \boldsymbol{n} = -1. \tag{4.3}$$

In this limit, the change of variables from the dimensionless temperature T to $T^\star$ given by (4.1) is translated to the definition of the temperature at the free surface as $\theta = (1 + Bi\theta^\star)/(1 + Bi)$. The approximation of the heat transfer at the interface leading from (4.2) to (4.3) can be readily applied in our formulation by expanding $\theta \approx 1 + Bi(\theta^\star - 1)$. A modified system of equations is then obtained simply by substituting $\theta^\star$ for θ in (1.1) and keeping the leading-order terms in Bi:

$$\partial_t h = -\partial_x q, \tag{4.4a}$$

$$\begin{aligned}\partial_t q = {} & \frac{9}{7}\frac{q^2}{h^2}\partial_x h - \frac{17}{7}\frac{q}{h}\partial_x q \\ & + \left\{\frac{5}{6}h - \frac{5}{2}\frac{q}{h^2} + 4\frac{q}{h^2}(\partial_x h)^2 - \frac{9}{2h}\partial_x q\,\partial_x h - 6\frac{q}{h}\partial_{xx}h + \frac{9}{2}\partial_{xx}q \right. \\ & \left. - \frac{5}{6}Bh\partial_x h + \frac{5}{6}\Gamma h\partial_{xxx}h - MaBi\left(\frac{5}{4}\partial_x\theta^\star - \frac{1}{224}hq\partial_{xx}\theta^\star\right)\right\} \\ & \times \left(1 - \frac{1}{70}q\partial_x h + MaBi\frac{5}{56h}\partial_x\theta^\star\right)^{-1},\end{aligned} \tag{4.4b}$$

$$\begin{aligned}Pr\partial_t\theta^\star = {} & 3\frac{(1-\theta^\star-h)}{h^2} + Pr\left[\frac{7}{40}\frac{(1-\theta^\star)}{h}\partial_x q - \frac{27}{20}\frac{q}{h}\partial_x\theta^\star\right] \\ & + \left(1 - \theta^\star - \frac{3}{2}h\right)\left(\frac{\partial_x h}{h}\right)^2 + \frac{\partial_x h\,\partial_x\theta^\star}{h} + (1-\theta^\star)\frac{\partial_{x^2}h}{h} + \partial_{xx}\theta^\star.\end{aligned} \tag{4.4c}$$

Now the Marangoni and Biot numbers appear through their product only, which reduces the number of relevant parameters by one and simplifies the parametric study of the nonlinear waves.

Another open question concerns large Péclet number flows. In this case the assumption of a small temperature gradient in the cross-stream direction is violated such that our three-variable model is no longer capable of describing accurately the wave dynamics. Nevertheless, a suggestion can be made. Indeed, our linear stability analysis and computations of solitary waves have suggested that more fields in addition to θ are necessary to correctly represent the heat transport process. In particular, we wish to overcome the spurious appearance of temperatures lower than the temperature of air that we observed for large-amplitude waves for sufficiently large Reynolds and Prandtl numbers. Hence, the aim would be to obtain reliable models, e.g. in terms of h, q, θ and t_1, compatible with the long-wave expansion up to second order, and which would also enable us to extend the present study to larger Péclet numbers. This and related issues will be addressed in a future study.

Despite the limitations of the regularized reduced model for large Péclet numbers, the model has substantially extended the region of validity of the Benney long-wave expansion which exhibits a turning point with branch multiplicity at an $O(1)$ value of Re, and for all Péclet numbers (see Kalliadasis *et al.* 2003), while in these regions our model has no turning points and predicts the continuing existence of solitary waves for all Reynolds numbers. Moreover, the appearance of unphysical negative temperatures at large Prandtl numbers is connected to the formation of recirculation zones in the solitary waves. Therefore, the regularized reduced model (1.1) should give results in reasonable agreement with experiments for waves of smaller amplitude for which no recirculation zones are observed.

C. R.-Q. and B. S. gratefully acknowledge fruitful discussions with Professor Paul Manneville. C. R.-Q. thanks Laurent Martin-Witkowski and Anne Sergent for their helpful comments. B. S. acknowledges support from European Union (Marie Curie contract HPMT-CT-2000-00207). This work has been facilitated by a CNRS/CGRI-FNRS cooperation. S. K. acknowledges financial support from EPSRC through an Advanced Research Fellowship, grant no. GR/S49520/01. The authors thank the Instituto Pluridisciplinar for hospitality.

REFERENCES

Alekseenko, S., Nakoryakov, V. & Pokusaev, B. 1994 *Wave Flow in Liquid Films*, 3rd Edn. Begell House.

Chang, H.-C. 1994 Wave evolution on a falling film. *Annu. Rev. Fluid Mech.* **26**, 103–136.

Davis, S. H. 1987 Thermocapillary instabilities. *Annu. Rev. Fluid Mech.* **19**, 403–435.

Doedel, E. J., Champneys, A. R., Fairgrieve, T. F., Kuznetsov, Y. A., Sandstede, B. & Wang, X.-J. 1997 Auto97: Continuation and bifurcation software for ordinary differential equations. *Tech. Rep.* Department of Computer Science, Concordia University, Montreal, Canada (available by FTP from `ftp.cs.concordia.ca` in directory `pub/doedel/auto`).

Gelndinning, P. & Sparrow, C. 1984 Local and global behavior near homoclinic orbits. *J. Statist. Phys.* **35**, 645–696.

Goussis, D. & Kelly, R. 1991 Surface wave and thermocapillary instabilities in a liquid film flow. *J. Fluid Mech.* **223**, 25–45, and corrigendum *J. Fluid Mech.* **226**, 663.

Joo, S. W., Davis, S. H. & Bankoff, S. G. 1991 Long-wave instabilities of treated falling films: two-dimensional theory of uniform layers. *J. Fluid Mech.* **230**, 117–146.

Kabov, O. A. 1996 Heat transfer from a small heater to a falling liquid film. *Heat Transfer Res.* **27**, 221–226.

Kabov, O. A., Marchuk, I. & Chupin, V. 1996 Thermal imaging study of the liquid film flowing on vertical surface with local heat source. *Russ. J. Engng Thermophys.* **6**, 105–138.

Kabov, O. A., Scheid, B., Sharina, I. & Legros, J. C. 2002 Heat transfer and rivulet structures formation in a falling thin liquid film locally heated. *Intl J. Thermal Sci.* **41**, 664–672.

Kalliadasis, S., Demekhin, E. A., Ruyer-Quil, C. & Velarde, M. G. 2003 Thermocapillary instability and wave formation on a film flowing down a uniformly heated plane. *J. Fluid Mech.* **492**, 303–338.

Keller, H. B. 1977 Numerical solution of bifurcation and nonlinear eigenvalue problems. In *Applications of Bifurcation Theory* (ed. P. H. Rabinowitz), pp. 359–384. Academic.

Ooshida, T. 1999 Surface equation of falling film flows which is valid even far beyond the criticality. *Phys. Fluids* **11**, 3247–3269.

Oron, A. & Gottlieb, O. 2002 Nonlinear dynamics of temporally excited falling liquid films. *Phys. Fluids* **14**, 2622–2636.

Pumir, A., Manneville, P. & Pomeau, Y. 1983 On solitary waves running down an inclined plane. *J. Fluid Mech.* **135**, 27–50.

Ruyer-Quil, C. & Manneville, P. 2000 Improved modeling of flows down inclined planes. *Eur. Phys. J.* B **15**, 357–369.

Ruyer-Quil, C., Scheid, B., Kalliadasis, S., Velarde, M. G. & Zeytounian, R. Kh. 2005 Thermocapillary long waves in a liquid film flow. Part 1. Low-dimensional formulation. *J. Fluid Mech.* **538**, 199–222.

Salamon, T., Armstrong, R. & Brown, R. 1994 Traveling waves on vertical films: Numerical analysis using the finite element method. *Phys. Fluids* **6**, 2202–2220.

Scheid, B., Ruyer-Quil, C., Thiele, U., Kabov, O., Legros, J. & Colinet, P. 2005 Validity domain of the Benney equation including Marangoni effect for closed and open flows.

Scriven, L. E. & Sternling, C. 1964 On cellular convection driven by surface-tension gradients: effects of mean surface tension and surface viscosity. *J. Fluid Mech.* **19**, 321–340.

Shkadov, V. Ya. 1967 Wave flow regimes of a thin layer of viscous fluid subject to gravity. *Izv. Ak. Nauk SSSR, Mekh. Zhi. Gaz* **2**, 43–51; English transl. *Fluid Dyn.* **2**, 29–34.

Shkadov, V. Ya. 1977 Solitary waves in a layer of viscous liquid. *Izv. Ak. Nauk SSSR, Mekh. Zhi. Gaz* **12**, 63–66; English transl. *Fluid Dyn.* **12**, 52–55.

Shraiman, B. I. 1987 Diffusive transport in a Rayleigh-Bénard convection cell. *Phys. Rev.* A **36**, 261–267.

Takashima, M. 1981 Surface driven instability in a horizontal liquid layer with a deformable free surface. *J. Phys. Soc. Japan* **50**, 2745–2756.

Trevelyan, P. M. J., Kalliadasis, S., Merkin, J. H. & Scott, S. K. 2002 Mass transport enhancement in regions bounded by rigid walls. *J. Engng Maths* **42**, 45–64.